Flexoelectric effects in a bent α-In_2Se_3 ferroelectric monolayer

Hongli Chen (陈红丽),[1] Chen Hu (胡尘),[1] Li Chen (陈立),[1] Liyuan Chen (陈丽媛),[1] Kai Jiang (姜凯),[2] Liangqing Zhu (朱亮清),[1] Liyan Shang (商丽燕),[1] Yawei Li (李亚巍),[1] Junhao Chu (褚君浩),[1] Shijing Gong (龚士静),[1,*] and Zhigao Hu (胡志高)[1,3,†]

[1]*Technical Center for Multifunctional Magneto-Optical Spectroscopy (Shanghai), Engineering Research Center of Nanophotonics & Advanced Instrument (Ministry of Education), Department of Physics, School of Physics and Electronic Science, East China Normal University, Shanghai 200241, China*

[2]*School of Arts and Sciences, Shanghai Dianji University, Shanghai 200240, China*

[3]*Collaborative Innovation Center of Extreme Optics, Shanxi University, Taiyuan, Shanxi 030006, China*

(Received 16 May 2024; accepted 25 June 2024; published 8 July 2024)

Flexoelectric effects in materials can bring novel physical properties that are absent in their perfect crystal, and have a wide range of applications, such as mechanical sensors and wrinkled triboelectric nanogenerators. In this work, electronic structures and transport properties of bended α-In_2Se_3 monolayer are investigated through first-principles calculations and nonequilibrium Green's function (NEGF). We find that two different kinds of type-II band structures can be obtained in $\widetilde{P}\uparrow$ and $\widetilde{P}\downarrow$ flexed α-In_2Se_3, which show opposite band bending. Carriers in the center of $\widetilde{P}\uparrow$ and $\widetilde{P}\downarrow$ flexed α-In_2Se_3 are mainly holes and electrons, respectively, which dominate the current behavior of the α-In_2Se_3 p-i-n (PIN) field-effect transistor (FET). The $\widetilde{P}\uparrow$ PIN-FET has enhanced forward current and the rectification ratio due to the larger density of holes. Our study achieves the homogeneous junction through bended α-In_2Se_3, which may simplify the device procession and be used as electromechanical sensors.

DOI: 10.1103/PhysRevB.110.014102

I. INTRODUCTION

The flexoelectric effect describes the phenomenon of electrode polarization caused by mechanical strain gradient or mechanical response caused by electric-field gradient. The flexoelectric effect is prevalent in all dielectric materials. Even when flexure is applied to a nonpiezoelectric material, its nonuniform strain can generate hundreds or thousands of volts per meter [1]. Recently, sensors [2], actuators [3], mechanical memories [4], and captive energizers [5] based on the flexoelectric effect have significant applications in fields, such as wearable electronics, crack monitoring, and structural health monitoring [6–9].

Conventional materials subjected to large stresses usually lead to surface fracture. However, two-dimensional (2D) materials have lower bending stiffness due to their single or few atomic layer thicknesses, which are more prone to flexing than conventional materials. The flexoelectric effect becomes more pronounced as the material size decreases [10–12]. With device refinement and the booming development of flexible devices [13–16], flexoelectric effects in 2D materials have attracted attention. For example, it is shown that the photocatalytic ability of carbon macrostructure (CN) nanosheets is significantly enhanced after flexure [17]. In bent VSe_2, the discontinuous and inhomogeneous strain gradient can dramatically change the magnetic moment of V atoms and induce out-of-plane polarization [18]. The overhanging channel of graphene in flexural devices can effectively avoid contact between the channel and the substrate, eliminating the negative effects brought by the substrate and significantly improving carrier mobility [19,20]. Recently, we have well quantified the flexoelectric-induced out-of-plane piezoelectric response in bent 2D materials [21]. Moreover, a general formula has been proposed to directly quantify the longitudinal flexoelectric coefficient, which is closely related to the flexural properties [22]. Also, we utilized the coupling of flexoelectric polarization and photogenerated carriers in a bent InSe channel to realize the synaptic device with excellent performance based on flexophotoelectronic effects [23], which further stimulates the potential of flexoelectricity in atomic-level materials.

As we know, applying nonuniform stress to bend the material produces strain fields in opposite directions on the top and bottom surfaces of the material. For 2D ferroelectric materials with out-of-plane polarization, there will be difference in the electronic density of states due to the different charge distributions on the top and bottom surfaces. Therefore, for 2D ferroelectrics, more interesting properties may emerge with the coupling of ferroelectric spontaneous polarization and flexural polarization. In addition, the physical mechanism of flexure's effect on the transport properties for devices has been still unknown. The relevant physical mechanisms are urgently needed to reference the experiments. As a member of the ferroelectric family, α-In_2Se_3 has superior properties, and its out-of-plane ferroelectric properties remain in the monolayer limit at room temperature [24–26]. α-In_2Se_3 has good carrier mobility [27] and is a promising alternative material

*Contact author: sjgong@ee.ecnu.edu.cn
†Contact author: zghu@ee.ecnu.edu.cn

for fabricating 2D devices. Flexing α-In_2Se_3 can effectively modulate its band-gap size [28]. The flexoelectric effect can also flip the direction of α-In_2Se_3 ferroelectric polarization [29,30].

In this work, the influence of flexoelectric and ferroelectric effects on the electronic properties and device transport properties of monolayer α-In_2Se_3 are investigated. It is found that flexures in α-In_2Se_3 form a type-II band alignment. The flexoelectric effect can enhance the current and rectification ratio in the devices. These findings offer new possibilities for the design of devices and are crucial for developing flexible devices.

II. CALCULATION DETAILS

Based on density-functional theory (DFT) and nonequilibrium Green's function (NEGF) methods, simulations of structure optimization, electronic properties, and device transport properties are performed by the Atomistix ToolKit (ATK) software package [31]. The ATK software is now widely used in simulation studies of low-dimensional materials [32–38]. For the solution of the Kohn-Sham equations, we adopt the generalized gradient approximation (GGA) in the Perdew-Burke-Ernzerhof (PBE) generalized form to describe the exchange-correlation potential. We use the SG15 pseudopotential to describe the interactions between the nucleus and the valence electrons. The linear combination of atomic orbitals (LCAO) is utilized to extend the valence-electron wave function. The real-space density grid cutoff energy is set to 80 Hartree. Considering the simulation of the transport properties of the device, we set the x axis and z axis as the periodic direction of the structure, and the y axis as the direction perpendicular to the structure, and set the vacuum layer larger than 45 Å in the nonperiodic y direction. As well as considering the dipole correction, which is used to eliminate the spurious interactions between the model and the "image." A k-point sampling of $15\times1\times15$ in the x, y, and z directions in the first Brillouin zone is used for structural optimization, $21\times1\times21$ k points are used for calculations of electronic properties, and $9\times1\times200$ are used for simulations of the device transport properties. All calculations in the study are based on a geometrical model optimized to act on each atom with a force less than 0.02 eV/Å and a total energy convergence criterion less than 10^{-4} eV per atom. At the same time, for simplicity, the Fermi level of the calculated result is set to zero.

The source (S)-drain (D) current can be calculated according to the Landauer-Büttiker equation when the bias voltage V_{ds} is applied to the device [34,39]:

$$I(V_{\rm ds}) = \frac{e}{h}\int_{\mu_{\rm R}}^{\mu_{\rm L}} T(E, V_{\rm ds})[f_{\rm R}(E-\mu_{\rm R}) - f_{\rm L}(E-\mu_{\rm L})]{\rm d}E, \tag{1}$$

where e and h are the electron charge and the Planck's constant, respectively, $\mu_L(\mu_R)$ is the chemical potential of the left (right) electrode, i.e., the source (drain) electrode, $T(E, V_{ds})$ is the bias-related transmission coefficient, $f_{R(L)} = \{1+\exp[(E-\mu_{R(L)})/k_B T_{R(L)}]\}^{-1}$ is the Fermi-Dirac distribution function of the R (L) electrode, $T_{R(L)}$ is the temperature of the R (L) electrode, k_B is the Boltzmann constant, and the average of the chemical potentials of the source and drain electrodes, i.e., the average Fermi level, is set to zero.

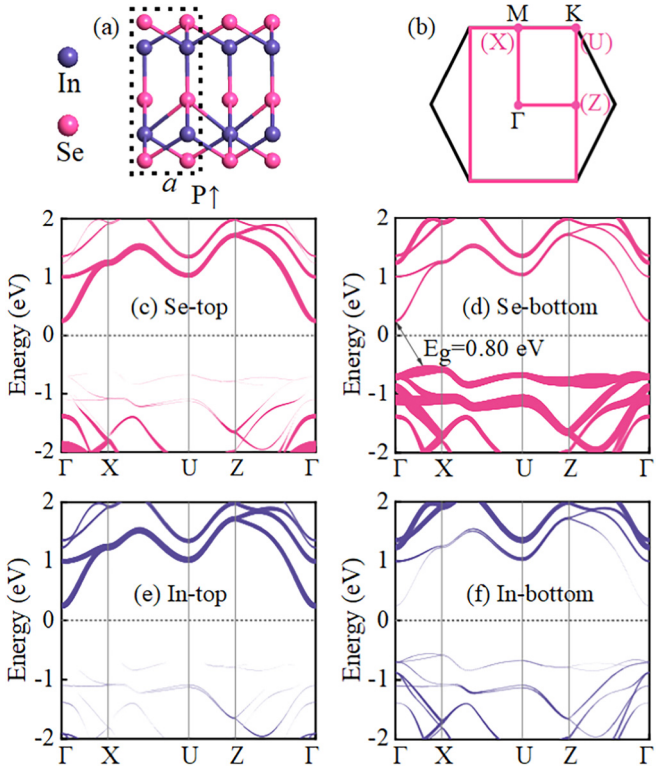

FIG. 1. Purple spheres indicate In atoms, magenta spheres indicate Se atoms. (a) Side view under the orthorhombic lattice of polarization-up ($P\uparrow$) α-In_2Se_3; (b) Brillouin zone of hexagonal and orthorhombic lattices; (c)–(f) Projected band structures of α-In_2Se_3.

III. RESULTS AND DISCUSSION

Monolayer α-In_2Se_3 has out-of-plane and in-plane spontaneous electrode polarization at room temperature. The side view of the structure is shown in Fig. 1(a), the lattice constant $a = 4.09$ Å of the structure-optimized α-In_2Se_3 unit cell, which is consistent with previous studies reported [40,41]. Monolayer α-In_2Se_3 has alternating Se-In-Se-In-Se layers, with two sublayers of In atoms. The top In atoms form a tetrahedral coordination with the four Se atoms in the vicinity, while the bottom In atoms form an octahedral coordination with the six Se atoms in the vicinity. The case can break space-inversion symmetry and induce the polarization. The intermediate Se atomic layer is biased toward the bottom In atomic layer for the polarization-up ($P\uparrow$) α-In_2Se_3. Conversely, the intermediate Se atomic layer in the polarization-down ($P\downarrow$) α-In_2Se_3 is relatively nearer to the top In atomic layer. The band structure is shown in Fig. 1(d), α-In_2Se_3 is indirect band-gap semiconductor with a band-gap value of 0.8 eV, which is in agreement with previous studies [40,41]. To facilitate the study of the flexoelectric effect of α-In_2Se_3 and its transport properties, the orthorhombic lattice is chosen as the base loss. The x axis is the armchair direction, and the z axis is the zigzag direction. The Brillouin zone of the hexagonal lattice and orthorhombic lattice is shown in Fig. 1(b). After the base loss changes

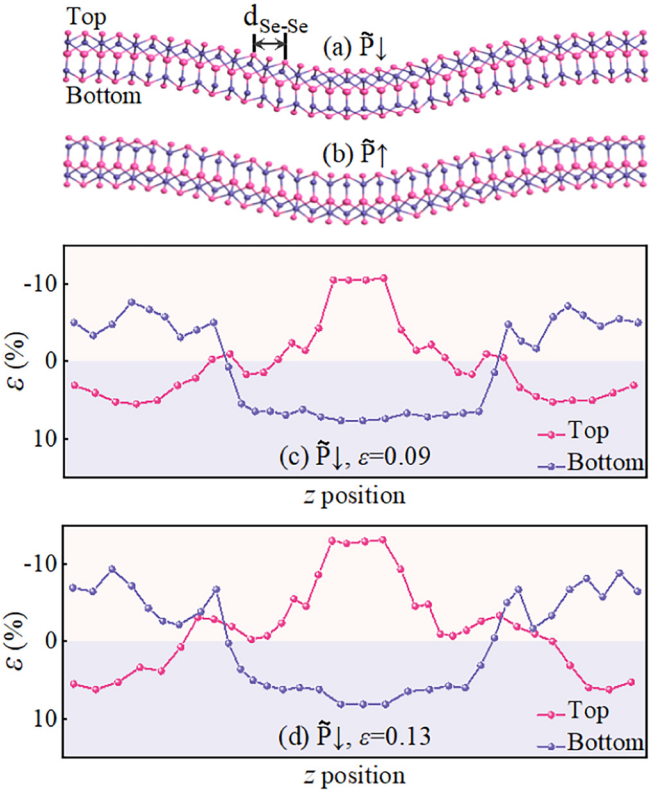

FIG. 2. (a) and (b) Side views of the $\widetilde{P}\downarrow$ and $\widetilde{P}\uparrow$ α-In_2Se_3, respectively; (c) and (d) Strain distributions on the top and bottom surface of the $\widetilde{P}\downarrow$ α-In_2Se_3 for $\varepsilon = 0.09$ and $\varepsilon = 0.13$, respectively.

into an orthorhombic lattice, the Brillouin zone path is Γ-X-U-Z-Γ. From the projected band structures of $P\uparrow$ α-In_2Se_3 in the orthorhombic lattice [Figs. 1(c)–1(f)], the In and Se atoms on the top surface jointly contribute to the conduction band. In contrast, the valence band is mainly contributed by Se atoms on the bottom surface.

Flexural structures can be achieved experimentally by placing the material on a waveform or circular hole-suspending substrate [21,42]. In the simulations, construct the α-In_2Se_3 flexural structure using a Gaussian function. As in Figs. 2(a) and (b), each unit cell is rotated sequentially by a certain angle from one end during cell expansion. The cells are expanded 18 times in the zigzag direction. The $P\uparrow$ and $P\downarrow$ α-In_2Se_3 flexures are denoted by $\widetilde{P}\uparrow$ and $\widetilde{P}\downarrow$ respectively. The degree of flexure is defined by $\varepsilon = (a\text{-}a_0)/a$, where a_0, a denote the lattice constants in the z-axis direction before and after flexure in the case of cell expansion, respectively.

The change in distance before and after the deflection of neighboring Se atoms on the same side of the top surface is defined as top strain. The change in the distance before and after the flexure of neighboring Se atoms is on the same side of the bottom surface as the bottom strain. Take $\widetilde{P}\downarrow$ α-In_2Se_3 in the $\varepsilon = 0.09$ and $\varepsilon = 0.13$ cases, the top and bottom strains distributed along the z direction are shown in Figs. 2(c) and (d). The top of the middle part of the material is subjected to large compressive stresses, while the bottom is subjected to tensile stresses. The top of the left and right ends are subjected to tensile stresses, and the bottom to compressive stresses. The top and bottom of the material are subjected to different stress fields, thus leading to the occurrence of strain gradients. The strain gradient increases with the flexure degree.

Figure 3(a) shows the partial charge-density distribution of flat $P\uparrow$ ($\overline{P}\uparrow$) α-In_2Se_3. The partial charge density corresponding to its valence-band maximum (VBM) is mainly concentrated on the lower side of the structure (i.e., the octahedral sublayer), which is provided primarily by Se atoms in the octahedral sublayer. However, the partial charge density corresponding to conduction-band minimum (CBM) is mainly concentrated in the upper side of the structure (that is, the tetrahedral sublayer), with a bit of distribution on the lower side. It is mainly provided by the In atoms in the tetrahedral sublayer and the Se atoms throughout the structure. Due to the proximity of In and Se atoms in tetrahedral coordination, there is a strong s-p hybridization between the In-s and Se-p orbitals. This forms the CBM as the antibonding state is pushed beyond the Fermi level. On the other hand, in the octahedral configuration, the Se atoms are spaced farther apart, resulting in weak p-p hybridization. As a result, their antibonding states do not cross the Fermi level, forming the VBM of α-In_2Se_3. After the polarization direction is flipped, due to the spatial inversion symmetry of α-In_2Se_3, the original band structure and charge distribution cannot be changed. The partial charge density corresponding to VBM is still concentrated in the octahedral sublayer. The partial charge density corresponding to CBM is still mainly focused on the tetrahedral sublayer, as shown in Fig. 3(b). However, after bending, the VBM and CBM corresponding to the structures with two different polarization directions show an interesting separation in real space. As shown in Fig. 3(c), after the $P\uparrow$ α-In_2Se_3 flexure, the partial charge density corresponding to its VBM is localized in the middle of the structure. The CBM corresponding partial charge densities are distributed at the left and right ends of the structure. In contrast, after the $P\downarrow$ α-In_2Se_3 flexure, the distribution of VBM and CBM in real space is exactly opposite to that after the $P\uparrow$ α-In_2Se_3 flexure. From Fig. 3(d), the partial charge density corresponding to its VBM is localized in the two ends of the structure. The middle of the structure provides the partial charge density corresponding to its CBM.

To gain insight into the effects caused by the flexoelectric effect on the material, the flexed α-In_2Se_3 structure is divided into 18 equal parts along the z-axis direction, labeling each part as z_1 to z_{18}. Figure 3(e) displays the density of states (DOS) of each part of $\widetilde{P}\uparrow$ α-In_2Se_3 at $\varepsilon = 0.13$. The middle part has an upward bending DOS, with its VBM closer to the Fermi level than the end part. Hence, the middle part forms p-type doping. The DOS of the two end parts shifts downward, resulting in a staggered type-II band alignment between the end and middle parts. From the statistical VBM and CBM positions of each part in Fig. 3(g), the two ends with the middle part produce a conduction-band offset of up to 0.58 eV. The value of the resulting valence-band offset is 0.28 eV. The huge conduction-band offset and valence-band offset can significantly increase the photogenerated carriers and prolong the exciton lifetime, which is very favorable for the design and application of exciton transport, photovoltaic devices, solar cells, and so on. The DOS for each part of $\widetilde{P}\downarrow$ α-In_2Se_3 with $\varepsilon = 0.13$ is shown in Fig. 3(f), where also forms the type-II band alignment after being subjected to the flexoelectric effect. The difference is the upward shift

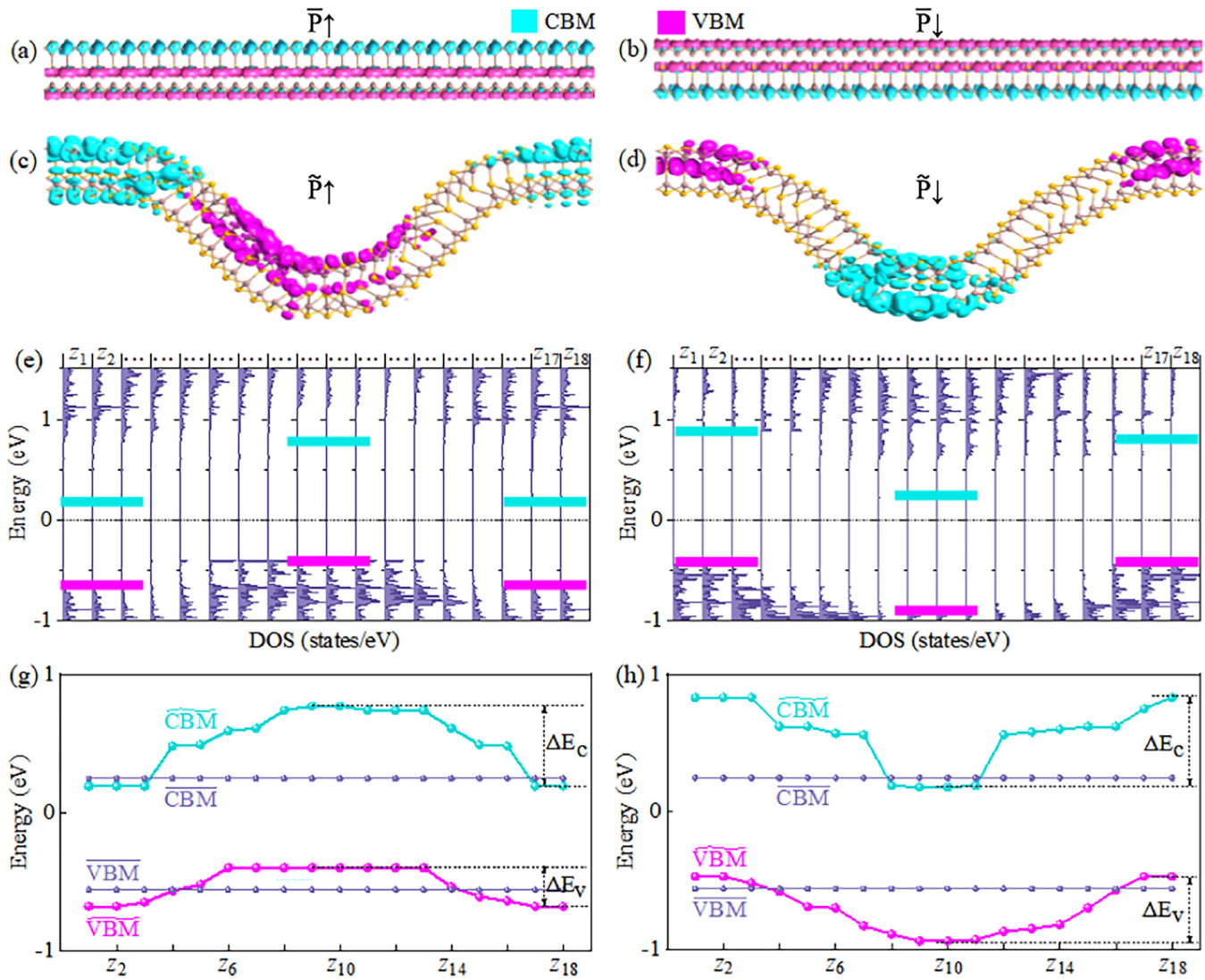

FIG. 3. VBM in magenta and CBM in cyan. CBM and VBM in real space for (a) $\overline{P}\uparrow$, (b) $\overline{P}\downarrow$, (c) $\widetilde{P}\uparrow$, and (d) $\widetilde{P}\downarrow$ α-In_2Se_3. (e) and (f) The segmented DOS of α-In_2Se_3 for $\widetilde{P}\uparrow$ and $\widetilde{P}\downarrow$ at $\varepsilon = 0.13$, respectively; the cyan solid line and magenta solid line indicate the locations of CBM and VBM, respectively. (g) and (h) The segmented CBM and VBM values of α-In_2Se_3 for $\widetilde{P}\uparrow$ and $\widetilde{P}\downarrow$ at $\varepsilon = 0.13$, respectively.

of the DOS in the two end parts, and the downward bending of the bands in the middle part. The middle part with the largest strain gradient constitutes the *n*-type doping. It means that the modulation of *p*-type and *n*-type doping can be achieved by bending α-In_2Se_3 with different out-of-plane polarizations.

Taking the $P\downarrow$ α-In_2Se_3 as an example, further analysis of the physical mechanism of the modulation of band structure changes by flexoelectric effects. Combined with Fig. 2(d), for $\widetilde{P}\downarrow$ α-In_2Se_3 with $\varepsilon = 0.13$, the different strain gradients result in a downward flexoelectric field E_{flex} at the left and right ends, and the direction of the flexoelectric field appearing in the middle portion is upward [11,43]. In addition, its out-of-plane dipole moment μ is downward. The dipole produces an additional electrostatic energy $W = -\mu \times E_{flex}$. As the middle and end portions of the material are subjected to flexoelectric fields in different directions, this leads to an increase in the energy of the middle portion and an upward shift of its Fermi level. A corresponding VBM and CBM shift down relative to the Fermi level causes the CBM and VBM in the middle part of $\widetilde{P}\downarrow$ α-In_2Se_3 with ε=0.13 to shift downward concerning $\overline{P}$, as shown in Fig. 3(h). As the energy at the left and right ends decreases, its Fermi level shifts downward. The corresponding VBM and CBM shift upward relatively. The flexoelectric field and ferroelectric polarization couple, leading to band-structure bending after α-In_2Se_3 flexure, forms far more valuable type-II band alignments.

PIN field-effect transistor (FET)-based $\overline{P}$, $\widetilde{P}\uparrow$, $\widetilde{P}\downarrow$ are designed. Figure 4(a) shows the schematic diagram of the device, which contains the left and right electrodes, and the scattering area in the middle region. The bended structures in Figs. 3(b) and 3(d) constitute the scattering region. The *n*- and *p*-doped monolayers of α-In_2Se_3 are set as semi-infinite-length electrodes. The electrodes are doped using the atomic charge compensation method [44–46], the left (right) electrode and its electrode extension area are doped with *p*(*n*)-type doping at a concentration of 8×10^{20} e/cm^3. The *z* direction is the device-transport direction.

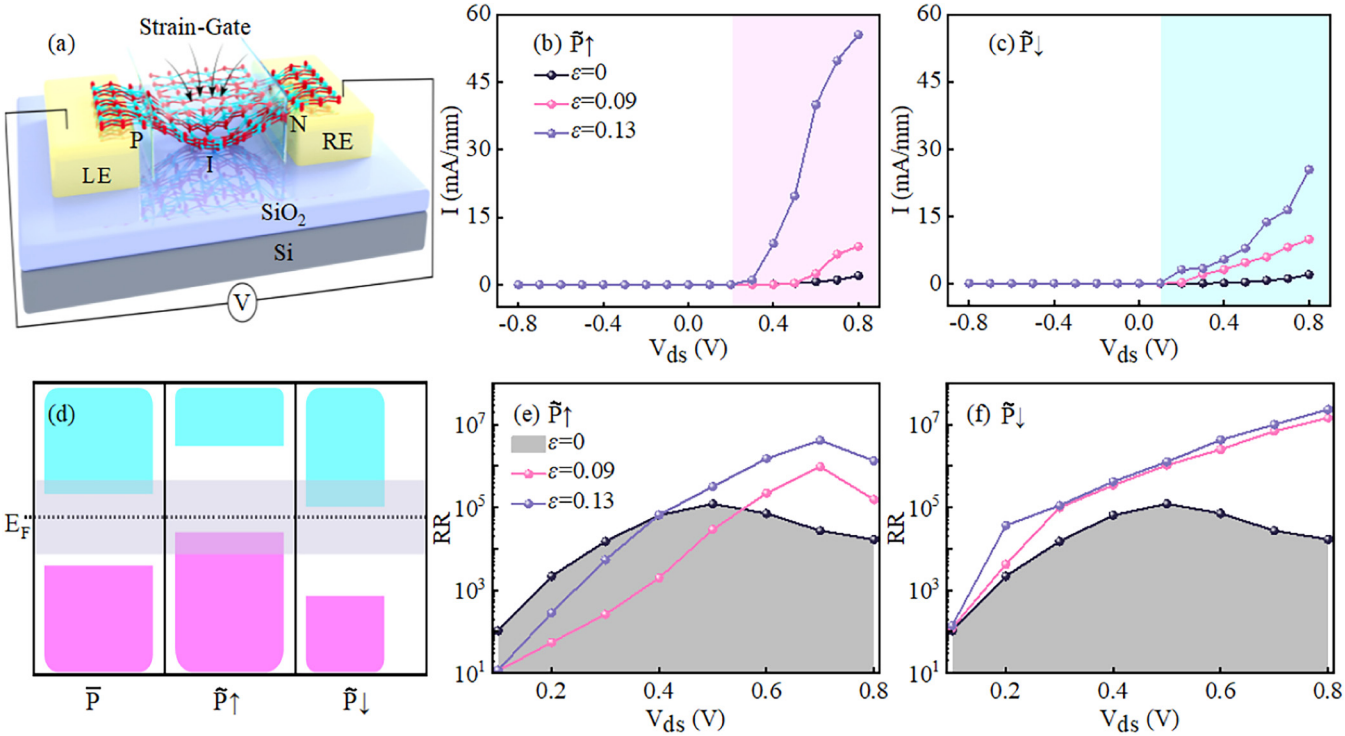

FIG. 4. (a) Schematic diagram of the device, in which LE is the left electrode, RE is the right electrode; I-V characteristic curves with $\varepsilon = 0$, $\varepsilon = 0.09$, and $\varepsilon = 0.13$ for (b) $\widetilde{P}\uparrow$ and (c) $\widetilde{P}\downarrow$; (d) Schematics of electronic structures and transport states involved in the device; (e) and (f) Rectification ratios at different flexure degrees for $\widetilde{P}\uparrow$ and $\widetilde{P}\downarrow$ α-In_2Se_3, respectively.

Using Eq. (1), the current of each device in the range of bias voltages from −0.8 V to 0.8 V can be calculated. At equal positive bias voltage, more significant deflection leads to higher current for $\widetilde{P}\uparrow$ and $\widetilde{P}\downarrow$ α-In_2Se_3 devices, as shown in Figs. 4(b) and (c). At a bias of 0.8 V, the source drain current of the $\overline{P}$ device is only 2.02 mA/mm, that of the $\widetilde{P}\downarrow$ device with ε=0.13 increases to 25.40 mA/mm. The $\widetilde{P}\uparrow$ device with ε=0.13 has a high current of 55.51 mA/mm, which is 27 times increase in current compared to the $\overline{P}$ device. At the same bias voltage, the device current increases with increasing flexure degree. As a result, the strain gradient generated by mechanical bending is similar to the gate, which can modulate the current size of the FET, figuratively known as the "strain-gate."

The different current of $\overline{P}$, $\widetilde{P}\uparrow$, $\widetilde{P}\downarrow$ can be well understood from their spation DOS in Figs. 3(e) and 3(f). For $\widetilde{P}\uparrow$-FET, VBM dominates the current, while for $\widetilde{P}\downarrow$-FET CBM does. Figure 4(d) visualizes the positional changes of the conduction and valence bands in the scattering region of the three types of devices at a bias of 0.6 V. $\widetilde{P}\uparrow$ device scattering region due to flexure, the band structure bends upwards, and the valence band is involved in the conductivity. Flexing causes the $\widetilde{P}\downarrow$ device scattering-region band structure to shift downward, and the conduction band enters the bias window. This greatly enhances the transmission performance of the flexure device, as the flexoelectric effect acts as a current amplifier for the device. The current of $\widetilde{P}\uparrow$ device is greater than that of $\widetilde{P}\downarrow$ device at the same flexure degree, because after flexure, only a tiny portion of the band structure in the scattering region of the $\widetilde{P}\downarrow$ device bends and enters the bias window. The vast majority of the valence bands in the scattering region of the $\widetilde{P}\uparrow$ device bend upwards, as seen by comparing Figs. 3(g) and 3(h). The CBM in the scattering region of $\widetilde{P}\downarrow$ device is nearer to the Fermi level relative to the VBM in the scattering region of $\widetilde{P}\uparrow$ device. It means that the CBM in the scattering region of the $\widetilde{P}\downarrow$ device enters the bias window faster after applying the bias. This also explains the phenomenon of $\widetilde{P}\downarrow$ device showing current at lower forward bias than $\widetilde{P}\uparrow$ device.

To further analyze the physical mechanism on the variation of the I-V characteristics for $\overline{P}$ device, $\widetilde{P}\uparrow$ device, and $\widetilde{P}\downarrow$ device, the projected local density of states (PLDOS) of the three types of devices with different bias voltages can be calculated, as shown in Fig. 5. Comparing the PLDOS of $\overline{P}$ device [Fig. 5(b)] and $\widetilde{P}\uparrow$ device [Fig. 5(e)] at $V_{ds} = 0$ V, due to the flexoelectric effect, the VBM position in the scattering region of the $\widetilde{P}\uparrow$ device is significantly nearer to the Fermi level relative to that of the $\overline{P}$ device scattering region. It means that under equal forward bias applied to the $\overline{P}$ and $\widetilde{P}\uparrow$ devices, as shown in Figs. 5(c) and 5(f), the density of states in the scattering region of the $\widetilde{P}\uparrow$ device move relatively more into the bias window. Thereby shortening the electron tunneling distance, resulting in a larger value of current. The band-edge variation of the $\widetilde{P}\uparrow$ device is extremely similar to the band-edge variation of the $\overline{P}$ device with negative gate voltage modulation. Similarly, for the $\widetilde{P}\downarrow$ device, when applying the positive bias voltage of 0.6 V [shown in Fig. 5(i)], the band structure near the CBM of the scattering region of the $\widetilde{P}\downarrow$ device is relatively more crowded into the bias window. The electron tunneling distance is shortened relative to the $\overline{P}$

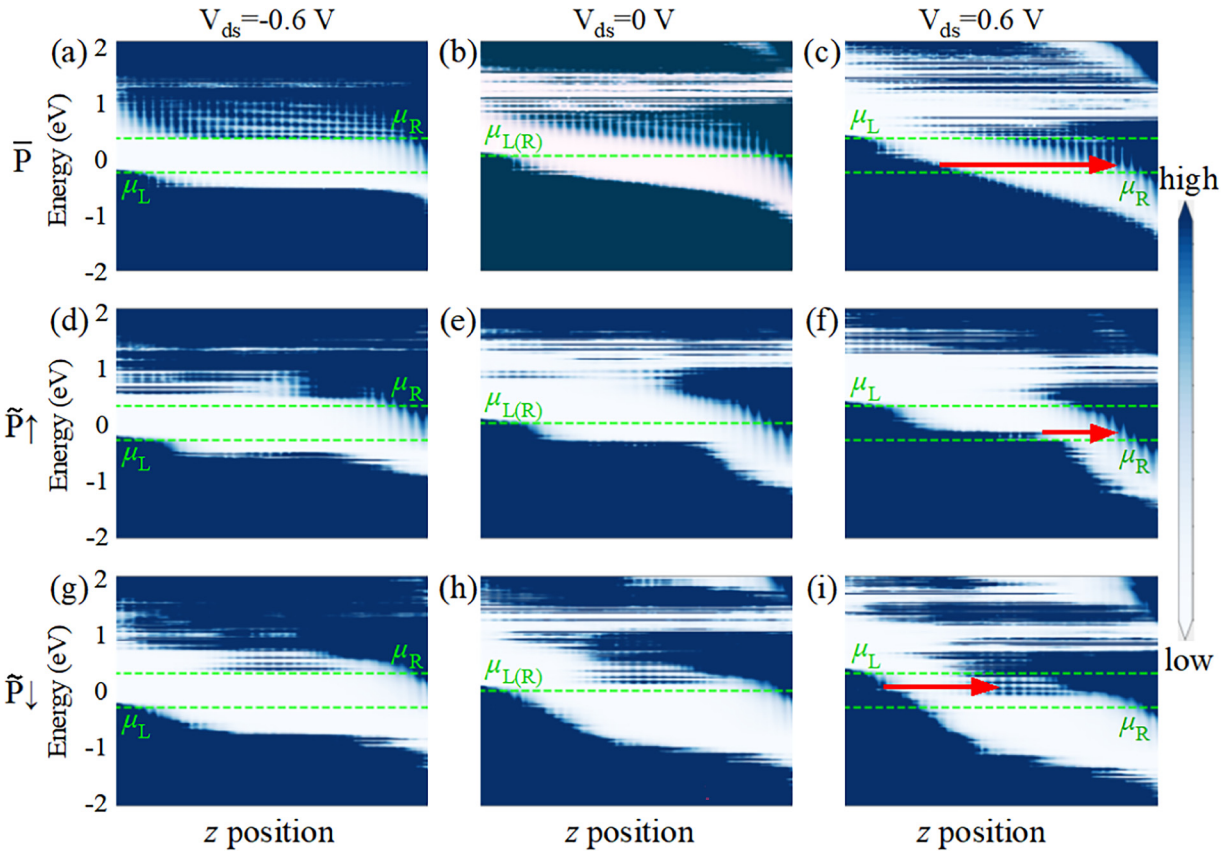

FIG. 5. PLDOS of $\overline{P}$-, $\widetilde{P}\uparrow$-, and $\widetilde{P}\downarrow$-PIN-FET with $V_{ds} = -0.6$ V, 0 V, and 0.6 V, respectively. The red arrow represents the tunneling distance.

device, and the current is relatively increased. In other words, by mechanical bending of $P\downarrow$ α-In_2Se_3, the regulatory effect of adding a positive gate voltage to the device is achieved. This phenomenon of the flexoelectric field generated by the strain gradient affecting the current size of the device can be imaginatively called the "strain-gate" regulatory behavior.

From Figs. 4(b) and 4(c), the currents of the $\overline{P}$ device, the $\widetilde{P}\uparrow$ device, and the $\widetilde{P}\downarrow$ device are all feeble under negative bias. Under the positive bias, the currents increase with increasing the positive bias, which shows prominent rectification characteristics. To quantify the rectification effect, the rectification ratio (RR) of the device is calculated [47]:

$$RR(V) = \frac{I(+V)}{I(-V)}. \tag{2}$$

For the $P\uparrow$ α-In_2Se_3 in Fig. 4(e), the rectification effect of the flexed device is better than that of the $\overline{P}$ device at high bias. For the $P\downarrow$ α-In_2Se_3 [Fig. 4(f)], the RR of the flexed devices are all higher than those of the unflexed devices. The highest RR of the $\overline{P}$ device is 10^5, while the highest RR of the $\widetilde{P}\downarrow$ device with $\varepsilon = 0.13$ can reach up 10^7. The RR of the $\widetilde{P}\downarrow$ device is upgraded by two orders of magnitude compared with that of the $\overline{P}$ device.

It is well known that when the bands of the source and drain electrodes overlap, and the overlap region is located in the bias window, the electrons from one side of the electrode can only pass through the center scattering region to reach the other side of the electrode, thus generating current [48,49]. Combined with PLDOS, the rectification characteristics of the device can be deeply understood. Taking the $\widetilde{P}\downarrow$ device as an example, in the case of -0.6 V [Fig. 5(g)], the left electrode potential decreases, the left electrode density of states moves overall to the low-energy range (downward). The right electrode potential is elevated, and the right electrode's band structure shifts upward relative to that of the right electrode under the 0 V bias. The left and right electrode band structures move downward and upward, decreasing the overlap of the left and right electrode band structures in the bias window. The transmission-restricted area becomes broader and the probability of electron tunnels plummets. Thus, the current is very weak at a bias of -0.6 V in the $\widetilde{P}\downarrow$ device. At a bias of 0.6 V [Fig. 5(i)], the left electrode potential increases while the right electrode potential decreases. This causes the band structure of the left electrode to shift upward and that of the right electrode to shift downward, increasing the overlap between both electrodes. It enhances the probability of electron tunneling from one electrode to the other, leading to a significant increase in current value. This is the reason why the $\widetilde{P}\downarrow$ device has a high RR.

IV. CONCLUSION AND OUTLOOK

In conclusion, through first-principle calculations, it is found that the flexoelectric effect brings novel physical properties to the material and enhances the device's performance. The physical mechanism of the action of the flexoelectric

effect is explained. Monolayer α-In_2Se_3 flexure leads to the separation of VBM and CBM in the real space of the material, constituting a homogeneous heterostructure with aligned type-II band alignment. This realizes the spatial separation of electron-hole pairs by simple mechanical bending. Due to the flexoelectric field and out-of-plane dipole coupling leading to the bending of the band structure, the forward current of the flexural device increases compared to the $\overline{P}$ device. At a bias of 0.8 V, the current in the flexure device is amplified by a factor of 27. Flexure exhibits "strain-gate" modulation behavior on the device. The RR of the flexed device reached 10^7. The results of this study show that flexure provides an innovative strategy for device performance enhancement. In addition, the study reveals the multiphysical field-coupling mechanism induced by the flexoelectric effect, which will facilitate the investigation and application of flexoelectric related technologies.

ACKNOWLEDGMENTS

This work was financially supported by the National Natural Science Foundation of China (Grants No. 62090013, No. 62274066, and No. 62375086), the National Key R&D Program of China (Grant No. 2019YFB2203403), the Projects of Science and Technology Commission of Shanghai Municipality (Grant No. 21JC1402100), and the Program for Professor of Special Appointment (Eastern Scholar) at Shanghai Institutions of Higher Learning.

[1] R. Maranganti, N. D. Sharma, and P. Sharma, Electromechanical coupling in nonpiezoelectric materials due to nanoscale nonlocal size effects: Green's function solutions and embedded inclusions, Phys. Rev. B **74**, 014110 (2006).

[2] Y. F. Zhang, Q. C. Lu, J. He, Z. H. Huo, R. H. Zhou, X. Han, M. M. Jia, C. F. Pan, Z. L. Wang, and J. Y. Zhai, Localizing strain via micro-cage structure for stretchable pressure sensor arrays with ultralow spatial crosstalk, Nat. Commun. **14**, 1252 (2023).

[3] S. W. Zhang, S. B. Shao, X. X. Yang, P. J. Chen, H. Ji, K. Y. Liu, T. H. Wu, S. P. Shen, and M. L. Xu, An enhanced flexoelectric dielectric elastomer actuator with stretchable electret, Smart Mater. Struct. **30**, 125004 (2021).

[4] H. Lu, C.-W. Bark, D. Esque De Los Ojos, J. Alcala, C. B. Eom, G. Catalan, and A. Gruverman, Mechanical writing of ferroelectric polarization, Science **336**, 59 (2012).

[5] J. K. Han, D. H. Jeon, S. Y. Cho, S. W. Kang, S. A. Yang, S. D. Bu, S. Myung, J. Lim, M. Choi, M. Lee, and M. K. Lee, Nanogenerators consisting of direct-grown piezoelectrics on multi-walled carbon nanotubes using flexoelectric effects, Sci. Rep. **6**, 29562 (2016).

[6] M. Wu, Z. Z. Jiang, X. J. Lou, F. Zhang, D. S. Song, S. C. Ning, M. Y. Guo, S. J. Pennycook, J. Y. Dai, and Z. Wen, Flexoelectric thin-film photodetectors, Nano Lett. **21**, 2946 (2021).

[7] X. N. Jiang, W. B. Huang, and S. J. Zhang, Flexoelectric nanogenerator: Materials, structures and devices, Nano Energy **2**, 1079 (2013).

[8] L. L. Shu, R. H. Liang, Z. G. Rao, L. F. Fei, S. M. Ke, and Y. Wang, Flexoelectric materials and their related applications: A focused review, J. Adv. Ceram. **8**, 153 (2019).

[9] W. T. Wu, L. L. Li, Z. X. Li, J. Z. Sun, and L. L. Wang, Extensible integrated system for real-time monitoring of cardiovascular physiological signals and limb health, Adv. Mater. **35**, 2304596 (2023).

[10] M. S. Majdoub, P. Sharma, and T. Cagin, Enhanced size-dependent piezoelectricity and elasticity in nanostructures due to the flexoelectric effect, Phys. Rev. B **77**, 125424 (2008).

[11] W. H. Ma, A study of flexoelectric coupling associated internal electric field and stress in thin film ferroelectrics, Phys. Status Solidi B **245**, 761 (2008).

[12] W. H. Ma, Flexoelectric charge separation and size dependent piezoelectricity in dielectric solids, Phys. Status Solidi B **247**, 213 (2010).

[13] S. J. Gong, C. Gong, Y. Y. Sun, W. Y. Tong, C. G. Duan, J. H. Chu, and X. Zhang, Electrically induced 2D half-metallic antiferromagnets and spin field effect transistors, Proc. Natl. Acad. Sci. USA **115**, 8511 (2018).

[14] S. F. Zhao, W. H. Ran, Z. Lou, L. L. Li, S. Poddar, L. L. Wang, Z. Y. Fan, and G. Z. Shen, Neuromorphic-computing-based adaptive learning using ion dynamics in flexible energy storage devices, Natl. Sci. Rev. **9**, 158 (2022).

[15] P. W. Guo, M. M. Jia, D. Guo, Z. L. Wang, and J. Y. Zhai, Retina-inspired in-sensor broadband image preprocessing for accurate recognition via the flexophototronic effect, Matter **6**, 537 (2023).

[16] M. Sharma, A. Singh, A. Kapoor, A. Singh, B. R. Tak, S. Kaushik, S. Bhattacharya, and R. Singh, Ultraflexible and transparent MoS_2/β-Ga_2O_3 heterojunction-based photodiode with enhanced photoresponse by piezophototronic effect, ACS Appl. Electron. Mater. **5**, 2296 (2023).

[17] H. T. Tan, W. P. Si, W. Peng, X. Chen, X. Q. Liu, Y. You, L. Q. Wang, F. Hou, and J. Liang, Flexo-/piezoelectric polarization boosting exciton dissociation in curved two-dimensional carbon nitride photocatalyst, Nano Lett. **23**, 10571 (2023).

[18] W. H. Shi, Y. F. Guo, Z. H. Zhang, and W. L. Guo, Strain gradient mediated magnetism and polarization in monolayer VSe_2, J. Phys. Chem. C **123**, 24988 (2019).

[19] K. I. Bolotin, K. J. Sikes, J. Hone, H. L. Stormer, and P. Kim, Temperature-dependent transport in suspended graphene, Phys. Rev. Lett. **101**, 096802 (2008).

[20] X. Du, I. Skachko, A. Barker, and E. Y. Andrei, Approaching ballistic transport in suspended graphene, Nat. Nanotechnol. **3**, 491 (2008).

[21] X. Wang, A. Y. Cui, F. F. Chen, L. P. Xu, Z. G. Hu, K. Jiang, L. Y. Shang, and J. H. Chu, Probing effective out-of-plane piezoelectricity in van der waals layered materials induced by flexoelectricity, Small **15**, 1903106 (2019).

[22] M. H. Deng, X. Wang, X. H. Xu, A. Y. Cui, K. Jiang, J. Z. Zhang, L. Q. Zhu, L. Y. Shang, Y. W. Li, Z. G. Hu, and J. H. Chu, Directly measuring flexoelectric coefficients μ_{11} of the van der Waals materials, Mater. Horiz. **10**, 1309 (2023).

[23] X. Wang, X. Zhou, A. Y. Cui, M. H. Deng, X. H. Xu, L. P. Xu, Y. Ye, K. Jiang, L. Y. Shang, L. Q. Zhu, J. Z. Zhang, Y. W. Li, Z. G. Hu, and J. H. Chu, Flexo-photoelectronic effect in *n*-type/*p*-type two-dimensional semiconductors and a deriving light-stimulated artificial synapse, Mater. Horiz. **8**, 1985 (2021).

[24] Y. Zhou, D. Wu, Y. H. Zhu, Y. J. Cho, Q. He, X. Yang, K. Herrera, Z. D. Chu, Y. Han, M. C. Downer, H. L. Peng, and K. J. Lai, Out-of-plane piezoelectricity and ferroelectricity in layered α-In_2Se_3 nanoflakes, Nano Lett. **17**, 5508 (2017).

[25] F. Xue, W. J. Hu, K.-C. Lee, L.-S. Lu, J. W. Zhang, H.-L. Tang, A. Han, W.-T. Hsu, S. B. Tu, W.-H. Chang, C.-H. Lien, J.-H. He, Z. D. Zhang, L.-J. Li, and X. X. Zhang, Room-temperature ferroelectricity in hexagonally layered α-In_2Se_3 nanoflakes down to the monolayer limit, Adv. Funct. Mater. **28**, 1803738 (2018).

[26] C. J. Cui, W.-J. Hu, X. X. Yan, C. Addiego, W. P. Gao, Y. Wang, Z. Wang, L. Z. Li, Y. C. Cheng, P. Li, X. X. Zhang, H. N. Alshareef, T. Wu, W. G. Zhu, X. Q. Pan, and L.-J. Li, Intercorrelated in-plane and out-of-plane ferroelectricity in ultrathin two-dimensional layered semiconductor In_2Se_3, Nano Lett. **18**, 1253 (2018).

[27] M. W. Si, A. K. Saha, S. J. Gao, G. Qiu, J. K. Qin, Y. Q. Duan, J. Jian, C. Niu, H. Y. Wang, W. Z. Wu, S. K. Gupta, and P. D. Ye, A ferroelectric semiconductor field-effect transistor, Nat. Electron. **2**, 580 (2019).

[28] J. X. Zhang, X. L. Zhang, Y. Wang, P. Cheng, B. J. Feng, K. H. Wu, Y. H. Lu, and L. Chen, Giant bandgap engineering in two-dimensional ferroelectric α-In_2Se_3, J. Phys. Chem. Lett. **13**, 3261 (2022).

[29] E. Han, S. M. Nahid, T. Rakib, G. Nolan, P. F. Ferrari, M. A. Hossain, A. Schleife, S. Nam, E. Ertekin, A. M. van der Zande, and P. Y. Huang, Bend-induced ferroelectric domain walls in α-In_2Se_3, ACS Nano **17**, 7881 (2023).

[30] D. Y. Bai, Y. H. Nie, J. Shang, J. X. Liu, M. H. Liu, Y. Yang, H. F. Zhan, L. Z. Kou, and Y. T. Gu, Ferroelectric domain and switching dynamics in curved In_2Se_3: First-principles and deep learning molecular dynamics simulations, Nano Lett. **23**, 10922 (2023).

[31] S. Smidstrup, T. Markussen, P. Vancraeyveld, J. Wellendorff, J. Schneider, T. Gunst, B. Verstichel, D. Stradi, P. A. Khomyakov, U. G. Vej-Hansen, M. E. Lee, S. T. Chill, F. Rasmussen, G. Penazzi, F. Corsetti, A. Ojanperä, K. Jensen, M. Palsgaard, U. Martinez, A. Blom, M. Brandbyge *et al.*, QuantumATK: An integrated platform of electronic and atomic-scale modelling tools, J. Phys.: Condens. Matter **32**, 015901 (2020).

[32] Y. P. An, Y. S. Hou, K. Wang, S. J. Gong, C. L. Ma, C. X. Zhao, T. X. Wang, Z. Y. Jiao, H. Y. Wang, and R. Q. Wu, Multifunctional lateral transition-metal disulfides heterojunctions, Adv. Funct. Mater. **30**, 2002939 (2020).

[33] H. L. Chen, L. Zhang, X. Q. Deng, L. Sun, Z. H. Zhang, and Z. Q. Fan, Edge chemistry and tensile strain effects on the magnetic properties of 1D VSe_2 structures, J. Mater. Chem. C **9**, 12904 (2021).

[34] Q. Liu, J. J. Li, D. Wu, X. Q. Deng, Z. H. Zhang, Z. Q. Fan, and K. Q. Chen, Gate-controlled reversible rectifying behavior investigated in a two-dimensional MoS_2 diode, Phys. Rev. B **104**, 045412 (2021).

[35] S. B. Fang, C. Yang, Q. H. Li, B. C. Wu, L. Q. Xu, S. Q. Liu, J. Yang, J. C. Ma, J. C. Dong, Y. Li, J. B. Yang, and J. Lu, Ferroelectric-tunable photoresponse in α-In_2Se_3 photovoltaic photodetectors: An Ab Initio Quantum transport study, Phys. Rev. Appl. **19**, 024024 (2023).

[36] H. L. Guo, Y. H. Yin, W. Yu, J. Robertson, S. Liu, Z. F. Zhang, and Y. Z. Guo, Quantum transport of sub-5 nm InSe and In_2SSe monolayers and their heterostructure transistors, Nanoscale **15**, 3496 (2023).

[37] H. L. Chen, J. N. Han, X. Q. Deng, Z. Q. Fan, L. Sun, and Z. H. Zhang, Vertical strain and twist induced tunability on electronic and optical properties of Janus HfSSe/SnC van der Waals heterostructure, Appl. Surf. Sci. **598**, 153756 (2022).

[38] X. He, W. Z. Li, Z. Gao, Z. H. Zhang, and Y. He, Achieving real Ohmic contact by the dual protection of outer layer atoms and surface functionalization in 2D metal Mxenes/$MoSi_2N_4$ heterostructures, J. Mater. Chem. C **11**, 4728 (2023).

[39] M. Büttiker, Y. Imry, R. Landauer, and S. Pinhas, Generalized many-channel conductance formula with application to small rings, Phys. Rev. B **31**, 6207 (1985).

[40] W. J. Ding, J. B. Zhu, Z. Wang, Y. F. Gao, D. Xiao, Y. Gu, Z. Y. Zhang, and W. G. Zhu, Prediction of intrinsic two-dimensional ferroelectrics in In_2Se_3 and other III_2-VI_3 van der Waals materials, Nat. Commun. **8**, 14956 (2017).

[41] B. Zhou, K. Jiang, L. Y. Shang, J. Z. Zhang, Y. W. Li, L. Q. Zhu, S. J. Gong, Z. G. Hu, and J. H. Chu, Enhanced carrier separation in ferroelectric In_2Se_3/MoS_2 van der Waals heterostructure, J. Mater. Chem. C **8**, 11160 (2020).

[42] K. Kim, Z. Lee, B. D. Malone, K. T. Chan, B. Alemán, W. Regan, W. Gannett, M. F. Crommie, M. L. Cohen, and A. Zettl, Multiply folded graphene, Phys. Rev. B **83**, 245433 (2011).

[43] C. C. Liu, S. L. Hu, and S. P. Shen, Effect of flexoelectricity on electrostatic potential in a bent piezoelectric nanowire, Smart Mater. Struct. **21**, 115024 (2012).

[44] Z. H. Li, J. N. Han, S. G. Cao, Z. H. Zhang, and X. Q. Deng, Physical properties of monolayer $Mn(BiTeS)_2$ and its applications in sub-3 nm spintronic devices, Phys. Rev. B **108**, 184413 (2023).

[45] D. Stradi, U. Martinez, A. Blom, M. Brandbyge, and K. Stokbro, General atomistic approach for modeling metal-semiconductor interfaces using density functional theory and nonequilibrium Green's function, Phys. Rev. B **93**, 155302 (2016).

[46] Y. Y. Pan, J. R. Dai, L. Xu, J. Yang, X. Y. Zhang, J. H. Yan, J. Z. Li, B. Shi, S. Q. Liu, H. Hu, M. B. Wu, and J. Lu, Sub-5-nm monolayer silicane transistor: A first-principles quantum transport simulation, Phys. Rev. Appl. **14**, 024016 (2020).

[47] Z. H. Li, J. N. Han, S. G. Cao, and Z. H. Zhang, NbS_2/$MoSi_2P_4$ van der Waals heterojunction: Flexibly tunable electrical contact properties and potential applications for Schottky junction devices, Appl. Surf. Sci. **636**, 157766 (2023).

[48] M. Srivastava, A. Srivastava, and S. K. Pandey, Suitability of graphene monolayer as sensor for carcinogenic heavy metals in water: A DFT investigation, Appl. Surf. Sci. **517**, 146021 (2020).

[49] R. Hu, Y. H. Li, Z. H. Zhang, Z. Q. Fan, and L. Sun, O-Vacancy-line defective Ti_2CO_2 nanoribbons: Novel magnetism, tunable carrier mobility, and magnetic device behaviors, J. Mater. Chem. C **7**, 7745 (2019).